

**Photoionization by an ultraintense laser field: Response of atomic xenon**

A. D. DiChiara, I. Ghebregziabher, J. M. Waesche, T. Stanev, N. Ekanayake, L. R. Barclay, S. J. Wells, A. Watts, M. Videtto, C. A. Mancuso, and B. C. Walker

*Department of Physics and Astronomy, University of Delaware, Newark, Delaware 19716, USA*

(Received 28 October 2009; published 27 April 2010)

We present energy- and angle-resolved photoionization from Xe in an ultrastrong laser field at  $10^{19}$  W/cm<sup>2</sup>. The observed yields are consistent with the tunneling ionization of Xe<sup>9+</sup> to Xe<sup>24+</sup>. However, energy and angle-resolved photoelectron spectra show differences for electrons whose final energies are above or below 0.5 MeV, which is approximately the ponderomotive energy at these intensities. Above 0.5 MeV, the observed photoelectron cutoff energy (between 1 and 1.35 MeV), photoelectron energy spectra, and the angle-resolved photoelectron azimuthal distributions agree with a model using tunneling ionization, multiple charge states, a classical relativistic continuum, and nonparaxial three-dimensional (3D) focused laser field. Below 0.5 MeV the yields and angular distributions observed indicate dynamics not included within a classical, single electron model of the interaction.

DOI: [10.1103/PhysRevA.81.043417](https://doi.org/10.1103/PhysRevA.81.043417)

PACS number(s): 32.80.Fb, 32.80.Rm, 32.80.Wr, 33.60.+q

**I. INTRODUCTION**

Over the past 20 years major advances in laser technology have made it possible to create intensities up to  $10^{21}$  W/cm<sup>2</sup> in a laser focus [1]. The electric field corresponding to this intensity is several hundred times the field binding the 1 s electron in H. These “ultrastrong” fields exceed the traditional strong field regime ( $10^{13}$  W/cm<sup>2</sup> to  $3 \times 10^{16}$  W/cm<sup>2</sup>) and push the physics into relativistic interactions ( $3 \times 10^{16}$  W/cm<sup>2</sup> to  $10^{20}$  W/cm<sup>2</sup>). Dynamics from the strong laser field such as rescattering, where a photoelectron is driven back toward its parent ion by the laser field to impact ionize a second electron [2] or recombine with the parent ion and emit high harmonic radiation [3,4], take on new aspects in the ultrastrong field. Ultrastrong field rescattering involves Lorentz deflection, an energy scale of order  $10^5$  eV, and the excitation of many electrons [5,6]. More broadly, ultrastrong field interactions give rise to high-energy particles such as electrons, protons, and neutrons [7–13]. Recent discoveries include the acceleration of electrons up to 1 GeV [14], protons up to 60 MeV [15], and heavy lead ions with energies as high as 400 MeV from laser-plasma interactions [16]. Among the generated particles, electron production is one of the most fundamental since other particles are strongly influenced by the relativistic electrons created in the ultrastrong laser field. In addition, the evolution from an atomic to a plasma response is smooth and a cogent description of photoelectrons from the atom response in ultrastrong fields is important to fully understand atomic clusters [17], high-density targets [18], collision-ionized electrons [19,20], inner-shell hole creation [21], radiation physics [22], and molecular physics [23].

The atomic response to intense electromagnetic fields can be understood by categorizing the interaction into (i) ionization and (ii) photoelectron continuum dynamics. A nonrelativistic field ionization model by Ammosov, Delone, and Krainov (ADK) [24] has been very successful in describing the sequential ionization of atoms in laser fields with intensities as high as  $10^{19}$  W/cm<sup>2</sup> [5]. Briefly, the ADK model gives the nonrelativistic ionization rate of the outermost electron in an atom or ion when it tunnels through the effective potential of the laser and the Coulomb potential of the ion. The electron dynamics subsequent to tunneling ionization

electron can be divided into two categories, namely relativistic and nonrelativistic, which are differentiated by the intensity of the ionizing laser and kinetic energy of the electron in continuum.

In traditional strong fields (e.g., up to  $10^{16}$  W/cm<sup>2</sup> at optical frequencies) experiments have verified the majority of the electrons released typically exhibit kinetic energies  $<200$  eV [25]. Since the electron’s kinetic energy is small compared to its rest mass energy, the dynamics are within the framework of nonrelativistic kinematics in a plane-wave laser field. The electron oscillates linearly along the laser electric field at the same frequency as the laser field. The ejected electron kinetic energy and the probability of the electron returning to its parent ion depend on the pulse duration and the phase of the laser field when the electron is ionized [26,27]. Precision measurements of photoelectron momentum and energy distributions have provided essential insight into these processes as well as multielectron dynamics in strong laser fields [2].

In ultrastrong laser fields electrons are accelerated to relativistic velocities. The force due to the magnetic field component of the laser field is no longer negligible and the motion of the electron is nonlinear. Recently, atomic measurements have demonstrated the production of relativistic electrons from atoms submitted to an ultrastrong field by direct measurement of the photoelectrons [28,29] and indirectly from Thomson radiation [30].

Achieving such ultrahigh intensities requires the laser field be tightly focused. The oscillation amplitude of an electron trajectory in a relativistic laser field is often, in fact, comparable to the laser focus size. Consequently, in addition to gaining drift kinetic energy due to its initial phase in the field, an electron can also attain an additional momentum from the ponderomotive force as it accelerates down the intensity “hill” created by the spatial variation of the laser field [31] as long as the electron ejection time from the focus is small compared to the pulse duration. Because of this, a traditional plane-wave approximation for the laser field is no longer adequate to describe photoelectron continuum dynamics in ultrastrong laser fields. To a leading order, the paraxial approximation for focused laser fields may be adopted to describe the resulting electron dynamics more accurately. In the paraxial

approximation, transverse field components are assumed while longitudinal components are set to zero. The Lorentz force due to transverse field components confines photoelectron dynamics to the plane containing the polarization-propagation axes. Within the paraxial approximation, a photoelectron born with zero kinetic energy has an emission angle and kinetic energy  $E_{\text{kin}}$  related by a parabolic relationship (i.e.,  $\tan(\theta) = \sqrt{2m_0c^2/E_{\text{kin}}}$  [28], where  $\theta$  is defined as the angle measured from the  $z$  axis or propagation direction of the laser). However, from the Coulomb gauge condition for the vector potential,  $A$ , ( $\partial_z A_z = -\nabla A_\perp$ ), it immediately follows that a three-dimensional (3D) field with longitudinal components is required to fully describe the focused laser field. Numerical simulations investigating electron dynamics in focused geometries have revealed the parabolic paraxial solution breaks down and photoelectrons with a given kinetic energy,  $E_{\text{kin}}$ , are ejected into a range of polar angles [32]. Moreover, even electrons born with zero initial velocity may exit in azimuthal angles  $\varphi \neq 0^\circ$  where  $\varphi$  is defined as the angle measured from the laser electric field.

The kinetic energy due to the ponderomotive potential of a charged particle in a linearly polarized, infinite plane wave in the frame of the oscillation center may be written as  $U_p = \sqrt{m_e^2 c^4 + 2m_e c^2 U_p^{\text{nr}} - m_e c^2}$  [33], where the nonrelativistic ponderomotive potential is  $U_p^{\text{nr}} = e^2 E_0^2 / 4m_e \omega^2$  and  $\omega$  is the angular frequency of the laser field. At an intensity of  $10^{19}$  W/cm<sup>2</sup>, for example, an 800 nm laser has a ponderomotive potential of 424 keV. In ultrafast, strong fields the final energy,  $E = m_e c^2 + e^2 A^2(\omega\tau_0)/(2m_e c^2)$ , for one-electron ionization in a linearly polarized field, is determined by the phase  $\omega\tau_0$  of the vector potential  $\mathbf{A}$  when the electron entered the continuum [34]. This description neglects the ponderomotive force gradient, which can contribute an additional maximum energy of  $U_p^{\text{nr}}$  [35], as well as the nonparaxial field terms discussed previously. Since the photoelectrons studied here range from keV to MeV, they may or may not leave the laser focus before the end of the laser pulse. No simple closed-form solution or atomic model for the photoelectron energy in an ultrastrong laser focus is known to exist at this time. Therefore, photoelectron measurements are needed to help address the basic physics of atomic ionization by ultrastrong fields as well as recently proposed ultra-intense laser acceleration methods, which make use of this information [36].

In this work, we use an ultrastrong laser field with linear (LP) and circular (CP) polarizations to ionize Xe gas at a very low density. The resulting electrons are measured as a function of intensity, energy, and angle with a dynamic range of four orders of magnitude. The measurements are compared to a 3D, relativistic, multiple charge state, semiclassical, single-electron model of ionization [37]. Measurements of angle-resolved and energy-resolved photoelectrons with kinetic energies  $>U_p$  are in reasonable quantitative agreement with the model, while electrons with final energies  $<U_p$  are different from calculated results, indicating additional physics beyond one-electron ionization. The comparison between the model and measurements highlight the success of relativistic extensions to the strong field model for the highest-energy photoelectrons, but also its failure to capture all of the ionization dynamics in ultrastrong fields.

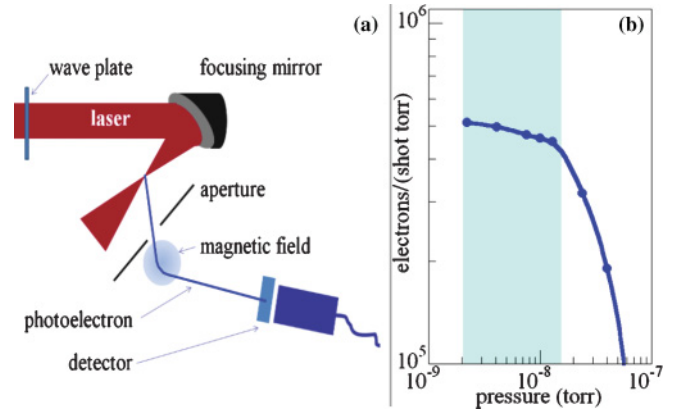


FIG. 1. (Color online) (a) Electron spectrometer. (b) Photoelectron-yield pressure dependence for 0.6 MeV LP light. The connecting line is to guide the eye and the highlighted region shows the pressure range at which the photoelectron collections were made.

## II. EXPERIMENTAL SETUP

Our experiment made use of an ultrafast, Ti:sapphire, terawatt, CPA laser system, described previously [38]. In brief, the laser system operates at a repetition rate of 10 Hz with TEM<sub>00</sub> spatial mode, pulse energies as high as 85 mJ with  $\pm 2.3\%$  energy fluctuations, and  $35 \pm 5$  fs pulse duration at a wavelength of 800 nm. A micro-optic lenslet array is used at the last amplification stage, a five-pass bow-tie amplifier, to spatially filter the pump beam and improve the mode quality [39].

The interaction chamber [Fig. 1(a)] consists of an ultrahigh vacuum (UHV) chamber coupled to a magnetic deflection spectrometer described in [40]. To ensure a well-defined gas interaction region and low background at the focus, the UHV chamber is differentially pumped by two turbo-molecular pumps to a base pressure better than  $10^{-9}$  torr. The laser polarization was changed using zero order  $\lambda/2$  and  $\lambda/4$  wave plates just before the UHV chamber. Tight focusing is achieved using a 3" diameter, 45° off-axis gold-coated parabolic mirror, which focuses the beam to a  $\sim 2 \mu\text{m}$  full width at half maximum (FWHM) diffraction-limited spot yielding a peak intensity  $>10^{19}$  W/cm<sup>2</sup>. Sample atoms of Xe are delivered to the interaction region through an effusive gas jet with 0.25 mm effective diameter at a very low density ( $10^9$  atoms/cm<sup>3</sup> to  $10^{11}$  atoms/cm<sup>3</sup>) to minimize space-charge effects. The peak intensity was confirmed with He photoelectron and Ar ion yield measurements to an accuracy of 50%.

The photoelectrons emitted from the laser focus enter the spectrometer by a 10-mm wide aperture that selects photoelectrons from a range of forward polar angles ( $\theta = 62^\circ \pm 5^\circ$ ) and azimuthal angles ( $\phi \pm 2^\circ$ ) to enter a pulsed magnetic field. The magnetic field deflects the measured electrons 40° from their original trajectory toward a fixed detector. The electromagnet is placed such that the magnetic field does not interact with photoelectrons prior to entering the spectrometer. Time of flight (TOF) with microchannel plates (MCP) coupled to a picosecond timing analyzer and discriminator was used to detect photoelectrons up to 250 keV. As the MCP's electron-detection efficiency decreases at high energies, a scintillator constructed from polyvinyl toluene

and organic fluors (Bicron 408) was used. The scintillator was coated with  $30 \pm 5$  nm of Al, deposited via a sputtering process, and given a border of colloidal graphite to ensure light tightness. The scintillator was used with a photomultiplier tube coupled to a digital phosphor oscilloscope for energies from 50 keV to 1.5 MeV. The oscilloscope utilized a dual condition trigger (amplitude and time windows) to collect the signal pulses. The spectrometer was calibrated using (1) TOF with the MCP detector to measure the electron velocity as a function of applied magnetic field, (2) pulse height analysis from the scintillator to corroborate the extrapolated fit line from MCP TOF and (3) 50 keV and 0.5 MeV radioactive  $\beta$  emitters placed near the laser focus. All the measurements were made with an energy resolution of  $\Delta E/E = 0.3$ .

To verify that plasma processes or collective and/or sample density effects did not contaminate the reported single-atom response, we verified all measurements exhibited a linear dependence on the Xe gas pressure. The photoelectron yield is linear with pressure for background pressures less than  $\sim 10^{-8}$  torr [Fig. 1(b)]. All collections reported here are free from anomalous pressure effects over one decade in pressure. The counting rates in the experiments were typically less than 0.1 detected events per laser shot. As an example, for 1 MeV photoelectron energies  $\sim 10$  events were recorded for 10 000 laser shots and at 60 keV  $\sim 100$  events were recorded for 3000 laser shots.

### III. EXPERIMENTAL RESULTS

#### A. Photoelectron yield intensity dependence

The intensity-dependent electron yields for Xe at a forward angle of  $\theta = 62^\circ$  with CP light are given in Fig. 2(b). The photoelectron energies analyzed were 60 keV and 0.6 MeV and the signal had a statistical fluctuation of 30% over several data acquisitions. The intensity dependence of photoelectron yields display a similar functional dependence with sequentially produced ion yields [41] with the region of unsaturated production that increases rapidly with intensity followed by the volume saturation of the laser focus, which proceeds by the well-known  $I^{3/2}$  scaling law. We start to detect photoelectrons with 60 keV at  $1.8 \times 10^{18}$  W/cm<sup>2</sup> and saturation is between  $2 \times 10^{18}$  W/cm<sup>2</sup> and  $3 \times 10^{18}$  W/cm<sup>2</sup>. The detection limit for 0.6 MeV is at about  $3 \times 10^{18}$  W/cm<sup>2</sup> ( $U^{\text{rel}}p = 155$  keV) and starts to saturate around  $7 \times 10^{18}$  W/cm<sup>2</sup>. A remarkable feature is the prominence of the 0.6 MeV photoelectron yield at an intensity of  $1.2 \times 10^{19}$  W/cm<sup>2</sup>, which is only about an order of magnitude below the lower energy (60 keV) photoelectron yield.

#### B. Energy and angle-resolved photoelectron spectra

The energy-resolved photoelectron spectra for a CP laser field with a peak intensity of  $1.2 \times 10^{19}$  W/cm<sup>2</sup> is shown in Fig. 3 in units of electron counts per laser shot into a keV energy bin at  $\theta = 62^\circ$ . The energy error bars represent the 30% uncertainty  $\Delta E/E$  of the spectrometer and a signal uncertainty factor of 3. The spectral amplitude is at a maximum for the lowest electron energy and decreases by a factor of  $10^3$  over the entire energy range. The maximum detected photoelectron energy is 1.35 MeV, which is about  $2.7U_p$ .

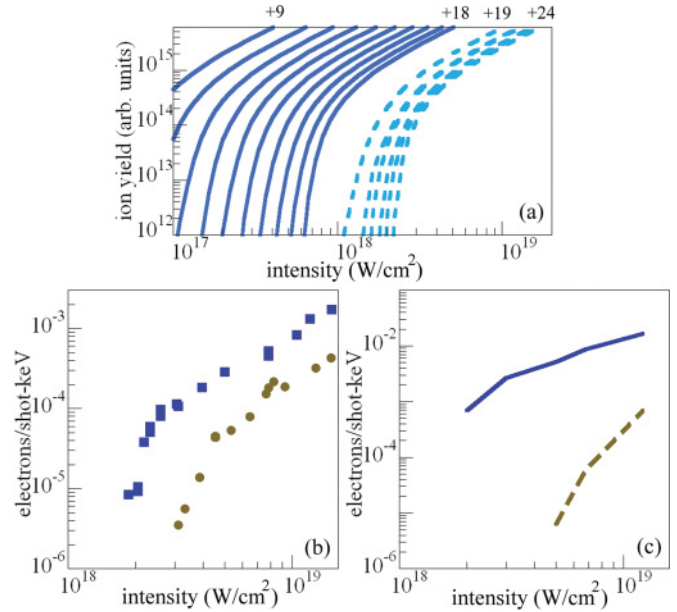


FIG. 2. (Color online) (a) Calculated ion yields for the charge states  $\text{Xe}^{9+}$  to  $\text{Xe}^{18+}$  (solid) and  $\text{Xe}^{19+}$  to  $\text{Xe}^{24+}$  (dashed). (b) Photoelectron intensity-dependent yields for CP light at 60 keV (blue squares) and 0.6 MeV (yellow circles). The calculated intensity-dependent yields at 60 keV (solid) and 0.6 MeV (dashed) are shown in (c).

Photoelectron angular distributions contain critical information about how electrons gain energy from the laser field and leave the laser focus. Therefore, to have a more detailed description of the single atomic response to relativistic laser fields, such as the initial photoelectron momentum at ionization and the final-state momentum, we measured photoelectron products with a linearly polarized ultrastrong laser field. Figures 4(a) and 4(b) show the energy spectra at azimuthal angles  $\phi = 0^\circ$  (in the direction of polarization) and  $\phi = 90^\circ$  (along  $\mathbf{B}_{\text{laser}}$ ) for an intensity of  $1.2 \times 10^{19}$  W/cm<sup>2</sup> at a forward angle of  $\theta = 62^\circ$ . Similar to the CP photoelectron energy spectrum, with LP the low-energy electrons have the highest probability of production; the electron yield decreases as the photoelectron energy increases. The maximum-detected photoelectron energy is 1.02 MeV at  $\phi = 0^\circ$  and 0.7 MeV

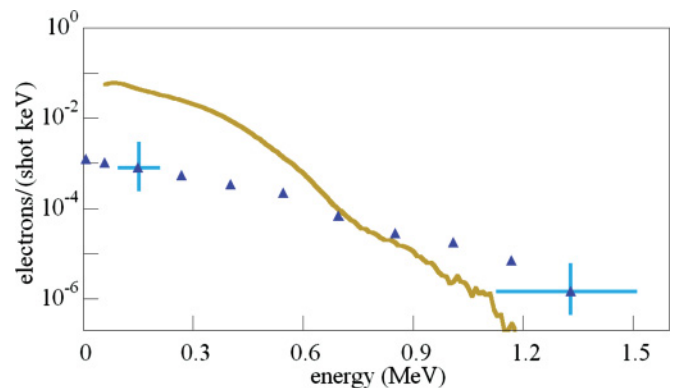


FIG. 3. (Color online) CP photoelectron energy spectrum at  $1 \times 10^{19}$  W/cm<sup>2</sup> for Xe with error bars and calculated spectrum from all charge states (line) with a model intensity of  $1.2 \times 10^{19}$  W/cm<sup>2</sup>.

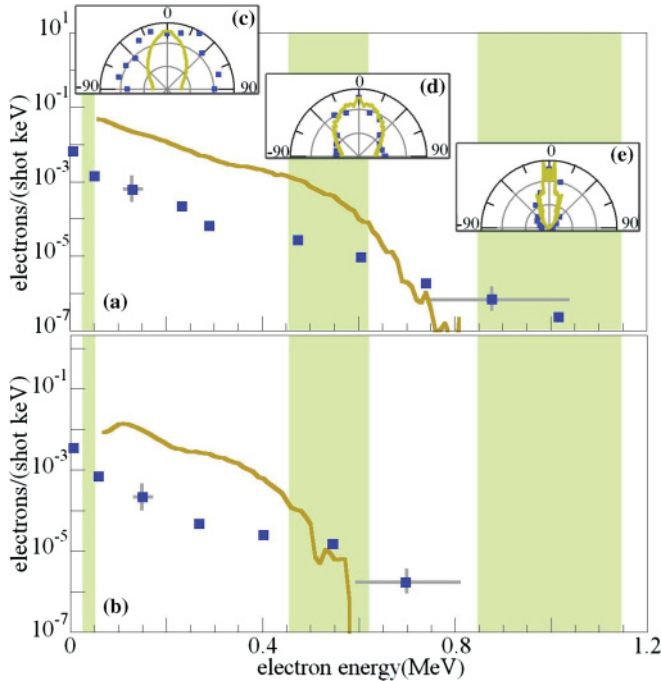


FIG. 4. (Color online) LP photoelectron energy spectrum at  $1 \times 10^{19}$  W/cm<sup>2</sup> with error bars and calculated spectrum (modeled at  $1.2 \times 10^{19}$  W/cm<sup>2</sup>) from all charge states (line) at a polar angle  $\theta = 62^\circ$  for (a)  $\phi = 0^\circ$  and (b)  $\phi = 90^\circ$ . The azimuthal angle distributions for (c) 60 keV, (d) 0.55 MeV, and (e) 1 MeV with the calculated values (line).

at  $\phi = 90^\circ$ . The azimuthal distributions for electrons with energies of 60 keV, 0.55 MeV, and 1 MeV [highlighted energy bands in Figs. 4(a) and 4(b)], are shown in Figs. 4(c) through 4(e), respectively. These azimuthal distributions indicate directional high-energy electrons and isotropic low-energy electrons. High-energy electrons have a higher probability of exiting the laser focus at an angle close to the plane containing  $\mathbf{E}_{\text{laser}}$  and the propagation axis.

#### IV. THEORETICAL MODEL

To better understand the relativistic production of photoelectrons from atoms submitted to ultrastrong laser fields, we used a 3D, relativistic, semiclassical, single-electron model of ionization described previously [37]. The model is used here as a “best effort” extension (we include, for example, a relativistic continuum, multiple charge states, and an accurate 3D laser focus) of the widely accepted and successful strong-field tunneling ionization model used at nonrelativistic intensities from  $10^{14}$  W/cm<sup>2</sup> to  $10^{16}$  W/cm<sup>2</sup> at optical frequencies [26,27]. Briefly, our model is a two-step process comprised of (i) ionization followed by (ii) continuum photoelectron dynamics. Starting with the neutral atom, the ionization rate is evaluated sequentially with respect to increasing charge. The rate equations are solved in time according to the calculations given by ADK [24], for each atom or ion across the laser focus. This method best represents the actual events within the laser focus for ionization from multiple charge states. However, these calculations are for single electrons and do

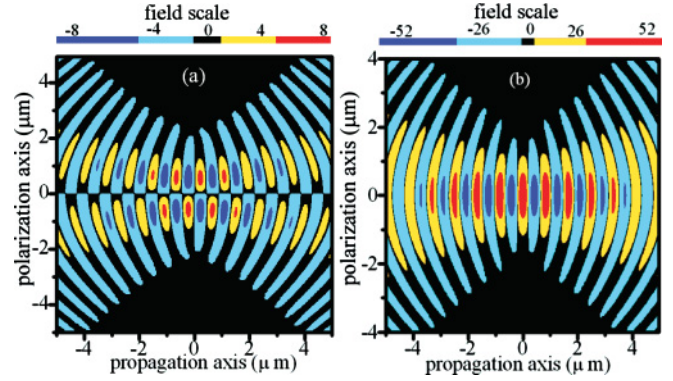


FIG. 5. (Color online) Contour plot of the spatial profile of (a)  $E_z(x, y = 0, z)$  and (b)  $E_x(x, y = 0, z)$  (with field strength given in atomic units) for a  $10^{20}$  W/cm<sup>2</sup> and  $1.6 \mu\text{m}$  beam diameter laser focus.

not account for multielectron phenomena (e.g., inner shell and Auger excitation).

Following tunneling is the second, continuum dynamics, step of the model. We use classical trajectory ensembles to simulate the tunneling photoionization current and continuum dynamics. Since the electron energy at the time of its birth is on the order of the ionization potential of the atomic or ionic species, the initial momentum of the electron is set to be zero. The laser pulse used for these calculations has an 800 nm center wavelength,  $f/\#2$  TEM<sub>00</sub> focus, 40 fs FWHM Gaussian temporal profile, and  $E_x$ ,  $E_y$ ,  $E_z$ ,  $B_x$ ,  $B_y$ , and  $B_z$  calculated exactly (i.e., nonparaxial [42,43] with corrections up to the third order). Better accuracy in the field calculation (i.e., higher-order corrections) do not change the presented results. Photoelectron dynamics are calculated by solving the relativistic equations of motion using a Runge-Kutta ordinary differential equation solver with a relative error tolerance threshold of  $10^{-6}$ , local error threshold of  $10^{-12}$ , and  $\sim 0.015$  fs time step. Including or excluding the Coulomb field of the core ion did not significantly affect the calculated dynamics. The calculation is considered in the low-density limit so space-charge effects are not included.

Among the nonparaxial corrections, the longitudinal field component  $\mathbf{E}_z$  is the largest. Figure 5 shows a contour plot of the nonparaxial field  $\mathbf{E}_z$  (a) and the transverse field component  $\mathbf{E}_x$  (b) for a linearly polarized laser focus with a beam diameter of FWHM  $\sim 1.6 \mu\text{m}$ . The figure shows longitudinal field components are not only nonzero, but also exhibit a different spatial profile compared to the transverse field component. The field component  $\mathbf{E}_z$  is asymmetric with respect to reflection about the polarization axis while  $\mathbf{E}_x$  preserves symmetry with reflection.  $\mathbf{E}_z$  vanishes along the axis (i.e., for  $x = 0, \mathbf{E}_z = 0$  while the amplitude of  $\mathbf{E}_x$  is at a maximum).

#### V. THEORETICAL RESULTS

Figure 2(a) depicts the calculated multiple charge-state ionization yields for Xe. These results show the ionization levels including a gap that occurs in Xe occurs between  $6 \times 10^{17}$  W/cm<sup>2</sup> ( $U_p = 36$  keV) and  $10^{18}$  W/cm<sup>2</sup> ( $U_p = 60$  keV) as the ionization state proceeds from the  $4d^{10}$  state with Xe<sup>18+</sup> to the  $4s^2 4p^6$  electrons with Xe<sup>19+</sup>. Compared to

Ar, where a similar intensity range includes a change in the ionization between the valence and  $L$  electron shells, the gap in the ionization rates is much smaller.

The calculated total photoelectron yield, which inputs the contribution from sequential ionization of all the ions in the full charge-state distribution across the focus is shown in Fig. 2(c). Except near the detection limit, the calculated results show reasonable quantitative agreement with the intensity dependence of the experimental data [Fig. 2(b)] within the 50% uncertainty in the intensity. Even though the intensity dependence of the calculated and experimental yields are similar, there is some disagreement about the relative quantity of 60 to 600 keV photoelectrons. The difference in yields at  $10^{19}$  W/cm<sup>2</sup> is about a factor of 30 for the calculations where the measured ratio is a factor of 5. At first this might seem obvious, since multielectron processes are not included in the theory. With CP light, however, multielectron processes such as rescattering are expected to shut down. The source of the disagreement is likely a small disagreement between the actual and calculated ionization rates; the sequential, one-electron tunneling rates used in the model slightly differ from the rates observed in the experiment.

The calculated energy-resolved photoelectron yield at  $1.2 \times 10^{19}$  W/cm<sup>2</sup> is shown in Fig. 3 with CP light. The energy distribution ranges from 50 keV (the lowest energy measured) to a cutoff at 1.35 MeV. Over this range the yield drops smoothly by about 1 decade per 0.5 MeV of energy. This can be compared to the strong field ionization response where the yield drops by three to four orders of magnitude as the photoelectron energy increases from 4 to 40 eV [44]. In Fig. 3 the experimental intensity of  $1 \times 10^{19}$  W/cm<sup>2</sup> is compared to calculations using a peak field intensity of  $1.2 \times 10^{19}$  W/cm<sup>2</sup>, well within the expected intensity error. The calculated highest detectable photoelectron energy is 1.2 MeV, which can be compared with the observed 1.35 MeV highest photoelectron energy to be well within the 30% uncertainty in the energy. Based on a best fit of the calculation to the data, low-energy photoelectrons predicted by the theory have yields greater than those observed in the experiment.

Figure 4 shows the angle-resolved photoelectron energy for an LP laser field at azimuthal angles (a)  $\phi = 0^\circ$  (along the  $\mathbf{E}_{\text{laser}}$ ) and (b)  $\phi = 90^\circ$  (along  $\mathbf{B}_{\text{laser}}$ ). As with the CP case, the experimental yield drops smoothly as a function of energy. At  $\phi = 0^\circ$  the drop is approximately 3 decades per MeV of energy while for  $\phi = 90^\circ$  the decrease is 4 decades per MeV. Three energy bands (50 to 70 keV, 0.47 to 0.63 MeV and 0.8 to 1.15 MeV), shown highlighted in Figs. 4(a) and 4(b), indicate the regions where the azimuthal distributions are collected. For the lowest energies (50 to 70 keV) the experimental distribution is nearly isotropic with only a 30% to 50% drop from  $\phi = 0^\circ$  to  $\phi = 90^\circ$ . Experimentally the azimuthal distribution gets more directional for increasing photoelectron energies. At 1 MeV the differences in the  $\phi = 0^\circ$  and  $\phi = 90^\circ$  yields is more than an order of magnitude. The experimental FWHM azimuthal angular emission for  $\sim 0.63$  MeV is  $103^\circ$  and  $53^\circ$  for  $\sim 1$  MeV. For energies near or above 0.63 MeV, the polar plots show excellent agreement between the calculated azimuthal distributions and those observed experimentally with the calculation also capturing the narrowing in the azimuthal angle as one goes to higher energies. The model

and experiment for the azimuthal distributions of the lowest energy ( $< 70$  keV) photoelectrons are not in agreement. The model shows the narrower azimuthal distribution expected also for strong field tunneling [25] while the azimuthal distribution in the experiments is more isotropic.

## VI. INTERPRETATION

Our model is able to successfully predict many of the observations in the experiment including the photoelectron yield dependence on laser intensity, photoelectron energy distribution, cutoff energy, and angular distributions above the ponderomotive energy for the photoelectron in the laser field. We begin our discussion with the intensity dependence of the photoelectron yield shown in Fig. 2(b). The break in the intensity dependence, which occurs at an event rate of about  $10^{-4}$  electrons/(shot keV) for both 60 keV and 0.6 MeV, distinguishes the boundary between the saturated and unsaturated regions for the ionization processes leading to these electron energies [45]. For larger species like Xe, more than a dozen charge states [see Fig. 2(a)] contribute to the ionization signal as the intensity increases to the ultrastrong field.

The sum of the ionization from multiple charge states factors into the total observed yield primarily at the intensity where their tunneling rate is the greatest and saturates. It is this charge-state distribution, the nonlinear appearance of any photoelectron energy, and saturation that gives the primary shape to the observed photoelectron energy distribution shown in Figs. 3 and 4(b) and 4(c). The impact of the charge-state distribution on the final photoelectron spectrum can also be seen in Ar [29] where the ionization at the same intensities as this study involves ionization from two different electron shells. Due to the large difference in the ionization rates between the  $L$  and valence shells, two components in the photoelectron spectrum can be easily identified as originating from photoelectrons from these two shells in Ar.

For the higher photoelectron energies, which come primarily from “ $4p$ ” electron states in Xe, the azimuthal emission angles [see Figs. 4(e) and 4(d)] calculated are in agreement with those observed. Since the initial energy of the photoelectron is assumed to be negligible in the calculations, it follows the energy and angular distribution for the highest-energy photoelectrons comes from the relativistic dynamics and acceleration of the photoelectron in the 3D laser focus.

For lower energies ( $\sim 60$  keV), which come from the ionization of the valence shell  $5s^2 5p^6$  and the  $4d^{10}$  electrons, the data shows a lower electron count than was expected for an azimuthal angle of  $\phi = 0^\circ$  (i.e., along the laser electric field). Much of the  $\phi = 0^\circ$  discrepancy in the yield between the model and experiment is actually representative of a disagreement in the azimuthal distribution for these 60 keV photoelectrons shown in Fig. 4(c) (i.e., the narrow distribution in  $\phi$  for the calculation and the isotropic  $\phi$  distribution observed give roughly the same  $\phi$  integrated counts). Photoelectron angular distributions contain critical information about how electrons gain energy from the field and leave the laser focus. The model neglects multielectron events, which could also give rise to the isotropic distribution seen in the data. Studies are underway to collect the data at a variety of forward angles ( $\theta$ ) to better

understand the sources of the isotropic photoelectrons and the physics behind the low-energy photoelectrons.

## VII. CONCLUSION

We have presented a measurement of relativistic, MeV photoelectron angular distributions from the single-atom photoionization of Xe exposed to field intensities as high as  $1.2 \times 10^{19}$  W/cm<sup>2</sup>. Photoelectrons with energies up to 1.35 MeV can be observed in the experiments. The primary features of the photoelectron spectrum above 0.5 MeV, including the intensity dependence, spectrum shape, high-energy cutoff, and azimuthal angular distributions, are in agreement with a relativistic, semiclassical, single-electron model of ionization that includes contributions to the ionization from multiple charge states and accounts for the involvement of the full 3D

focused laser field in the dynamics. The agreement indicates high-energy electrons in the MeV range are produced through tunneling ionization followed by 3D relativistic dynamics involving the full focal volume.

For energies below 0.5 MeV, the intensity dependence is qualitatively correct, but the yield and angular distributions are not fully addressed by extending the one-electron strong field model to the ultrastrong field. The existence of multielectron and high-energy atomic excitation processes not included in the model may be the cause behind the observed isotropic azimuthal distributions.

## ACKNOWLEDGMENTS

This material is based upon work supported by the Army Research Office under Award No. W911NF-09-1-0390 and the National Science Foundation under Award No. 0757953.

- 
- [1] G. A. Mourou, C. P. J. Barty, and M. D. Perry, *Phys. Today* **51**, 22 (1998).
  - [2] B. Walker, B. Sheehy, K. C. Kulander, and L. F. DiMauro, *Phys. Rev. Lett.* **77**, 5031 (1996).
  - [3] K. J. Schafer, B. Yang, L. F. DiMauro, and K. C. Kulander, *Phys. Rev. Lett.* **70**, 1599 (1993).
  - [4] W. P. Leemans *et al.*, *Nature Physics* **2**, 696 (2006).
  - [5] E. A. Chowdhury, C. P. J. Barty, and B. C. Walker, *Phys. Rev. A* **63**, 042712 (2001).
  - [6] K. Yamakawa, Y. Akahane, Y. Fukuda, M. Aoyama, N. Inoue, H. Ueda, and T. Utsumi, *Phys. Rev. Lett.* **92**, 123001 (2004).
  - [7] T. Ditmire *et al.*, *Nature (London)* **398**, 489 (1999).
  - [8] G. Malka and J. L. Miquel, *Phys. Rev. Lett.* **77**, 75 (1996).
  - [9] K. Krushelnick *et al.*, *Phys. Rev. Lett.* **83**, 737 (1999).
  - [10] E. L. Clark *et al.*, *Phys. Rev. Lett.* **84**, 670 (2000).
  - [11] G. Pretzler *et al.*, *Phys. Rev. E* **58**, 1165 (1998).
  - [12] M. D. Perry *et al.*, *Rev. Sci. Instrum.* **70**, 265 (1999).
  - [13] H. Schwörer, P. Gibbon, S. Dusterer, R. Behrens, C. Ziener, C. Reich, and R. Sauerbrey, *Phys. Rev. Lett.* **86**, 2317 (2001).
  - [14] W. P. Leemans *et al.*, *Nature Physics* **2**, 696 (2006).
  - [15] L. Robson *et al.*, *Nature Physics* **3**, 58 (2007).
  - [16] E. L. Clark, K. Krushelnick, M. Zepf, F. N. Beg, M. Tatarakis, A. Machacek, M. I. K. Santala, I. Watts, P. A. Norreys, and A. E. Dangor, *Phys. Rev. Lett.* **85**, 1654 (2000).
  - [17] T. Ditmire, J. W. G. Tisch, E. Springate, M. B. Mason, N. Hay, J. P. Marangos, and M. H. R. Hutchinson, *Phys. Rev. Lett.* **78**, 2732 (1997).
  - [18] P. A. Norreys *et al.*, *Phys. Rev. Lett.* **76**, 1832 (1996).
  - [19] A. Dorn, A. Kheifets, C. D. Schroter, B. Najjari, C. Hohn, R. Moshhammer, and J. Ullrich, *Phys. Rev. Lett.* **86**, 3755 (2001).
  - [20] R. Moshhammer *et al.*, *Opt. Express* **8**, 358 (2001).
  - [21] A. Becker *et al.*, *J. Phys. B* **33**, L547 (2000).
  - [22] J. Peatross, C. Muller, K. Z. Hatsagortsyan, and C. H. Keitel, *Phys. Rev. Lett.* **100**, 153601 (2008).
  - [23] S. Palaniyappan, R. Mitchell, R. Sauer, I. Ghebregziabher, S. L. White, M. F. Decamp, and B. C. Walker, *Phys. Rev. Lett.* **100**, 183001 (2008).
  - [24] M. V. Ammosov, N. B. Delone, and V. P. Krainov, *Zh. ksp. Teor. Fiz.* **91**, 2008 (1986) [*Sov. Phys. JETP* **64**, 1191 (1986)].
  - [25] B. Walker, B. Sheehy, K. C. Kulander, and L. F. DiMauro, *Phys. Rev. Lett.* **77**, 5031 (1996).
  - [26] P. B. Corkum, *Phys. Rev. Lett.* **71**, 1994 (1993).
  - [27] B. Yang *et al.*, *Acta Phys. Pol. A* **86**, 41 (1994).
  - [28] C. I. Moore, A. Ting, S. J. McNaught, J. Qiu, H. R. Burris, and P. Sprangle, *Phys. Rev. Lett.* **82**, 1688 (1999).
  - [29] A. D. DiChiara, I. Ghebregziabher, R. Sauer, J. Waesche, S. Palaniyappan, B. L. Wen, and B. C. Walker, *Phys. Rev. Lett.* **101**, 173002 (2008).
  - [30] S. Y. Chen, A. Maksimchuk, and D. Umstadter, *Nature (London)* **396**, 653 (1998).
  - [31] R. R. Freeman, P. H. Bucksbaum, H. Milchberg, S. Darack, D. Schumacher, and M. E. Geusic, *Phys. Rev. Lett.* **59**, 1092 (1987).
  - [32] S. X. Hu and A. F. Starace, *Phys. Rev. Lett.* **88**, 245003 (2002).
  - [33] D. Bauer, P. Mulser, and W. H. Steeb, *Phys. Rev. Lett.* **75**, 4622 (1995).
  - [34] P. B. Corkum, N. H. Burnett, and F. Brunel, *Phys. Rev. Lett.* **62**, 1259 (1989).
  - [35] B. Quesnel and P. Mora, *Phys. Rev. E* **58**, 3719 (1998).
  - [36] S. X. Hu and A. F. Starace, *Phys. Rev. Lett.* **88**, 245003 (2002).
  - [37] I. Ghebregziabher and B. C. Walker, *Phys. Rev. A* **76**, 023415 (2007).
  - [38] J. Z. H. Yang and B. C. Walker, *Opt. Lett.* **26**, 453 (2001).
  - [39] A. D. DiChiara *et al.*, *Opt. Lett.* **28**, 2106 (2003).
  - [40] G. E. Ongadi, M.S. thesis, University of Delaware, 2006.
  - [41] S. Palaniyappan *et al.*, *J. Phys. B* **39**, S357 (2006).
  - [42] L. W. Davis, *Phys. Rev. A* **19**, 1177 (1979).
  - [43] M. Lax, W. H. Louisell, and W. B. McKnight, *Phys. Rev. A* **11**, 1365 (1975).
  - [44] F. Grasbon, G. G. Paulus, H. Walther, P. Villoresi, G. Sansone, S. Stagira, M. Nisoli, and S. De Silvestri, *Phys. Rev. Lett.* **91**, 173003 (2003).
  - [45] A. DiChiara, I. Ghebregziabher, S. Palaniyappan, E. L. Huskins, A. Falkowski, D. Pajerowski, and B. C. Walker, *Progress in Ultrafast Intense Laser Science III*, edited by K. Yamanouchi, S. L. Chin, P. Agostini, and G. Ferrante (Springer-Verlag, Berlin, Heidelberg, 2008), pp. 53–74.